Mechanical Engineering and Materials Science Independent Study

Mechanical Engineering & Materials Science

5-23-2024

Investigating the Behavior of Ternary NbVZr Alloy and the Effect of Zr Addition on the Mechanical and Microstructural Properties

Caelyn Walton-Macaulay
Washington University in St. Louis

Recommended Citation

Walton-Macaulay, Caelyn, "Investigating the Behavior of Ternary NbVZr Alloy and the Effect of Zr Addition on the Mechanical and Microstructural Properties" (2024). *Mechanical Engineering and Materials Science Independent Study*. 258.
https://openscholarship.wustl.edu/mems500/258

Washington University in St. Louis
JAMES MCKELVEY SCHOOL OF ENGINEERING

Fall 2023-Spring 2024 MEMS 500 Independent Study

Investigating the Behavior of Ternary NbVZr Alloy and the Effect of Zr Addition on the Mechanical and Microstructural Properties

Instructor: Dr. Katharine M. Flores

Written By: Caelyn Walton-Macaulay

Date: Sunday, May 12, 2024

ABSTRACT: This study investigates the microstructural and compositional evolution of a ternary NbVZr alloy under varying Zr concentrations, utilizing scanning electron microscopy (SEM) imaging and energy-dispersive X-ray spectroscopy (EDS) analysis. Results show consistent overall composition across different Zr concentrations, with observable Zr-enriched regions decreasing in frequency with increasing Zr content, potentially due to destabilization effects. Microstructural analysis reveals an increase in the area fraction occupied by dendrites as Zr content increases, prompting a decrease in the interdendritic phase. A comparison with an active concurrent work on the deposition of Nb to the ternary alloy highlights similarities and differences in phase distribution and composition between the two conditions. Ternary diagrams analyses indicate that while the phases in the Zr-deposit are stable, they do not meet the criteria for the formation of a single-phase BCC solid solution.

INTRODUCTION AND BACKGROUND

The field of study involving the creation and manipulation of metallic alloys has been well established for decades. Conventional alloys usually consist of two elements; one metal makes up the primary or dominant phase, and the second element is interspersed throughout in smaller quantities [1, 2]. A familiar example of such an alloy is carbon steel- an iron based alloy with varying quantities of carbon interstitials, altering the properties of the base iron.

Recent work has begun to explore the formation and use of alloys composed of multiple metals in near-equal quantities, called Multi-Principle Element Alloys (MPEAs). High Entropy Alloys (HEAs) are a subset of MPEAs with 5 or more elements that form a single-phase solid solution; the name comes from the materials' high entropy as a result of the combination of equal or near-equal quantities of so many elements [2, 3]. HEAs possess many desirable qualities, including resistance to wear, durability in high-temperature environments, and resistance to oxidation or corrosion [4]. These properties can be difficult to find in conventional alloys. HEAs and MPEAs in general therefore are much more versatile materials. MPEAs can be designed and tailored to meet specific requirements for a wide range of applications.

The higher mixing entropy in these alloys has been found to facilitate the formation of a simple solid solution phase. The Gibbs free energy decreases as entropy increases, which stabilizes the solid solution phase. With more of this phase, the overall number of present phases decreases, yielding a more consistent material with the unique combination of properties that is characteristic of MPEAs [4]. The properties of an MPEA are primarily dependent on the atomic structure and phase composition of the material. The solid solution phase of the ternary alloy centered in this paper has been found to be a disordered BCC structure. The semi-random distribution of atoms creates a structure that inhibits dislocation motion, resulting in high strength and resistance to deformation [5].

Previous work by Li in 2022 found that the dendritic microstructure of the ternary NbVZr alloy consists of a BCC solid solution and two Laves structures forming in the interdendritic regions, which act as obstacles to dislocation motion in the dendrites and strengthen the alloy [6]. Therefore, for example, a NbVZr alloy with higher quantities of the interdendritic Laves phases is expected to exhibit higher hardness.

This work seeks to characterize the mechanical and microstructural properties of a ternary NbVZr alloy. It investigates how the addition of Zr to a ternary NbVZr alloy affects the formation of secondary phases and the mechanical properties associated with them. This paper is written in conjunction with another that investigates the addition of Nb instead of Zr [7].

METHODS

Making buttons. A final mass of 15g was assumed for each button. The equiatomic composition for each button of NbVZr alloy was calculated accordingly. Each button theoretically had 5.928g Nb, 3.251g V, and 5.821g Zr. The appropriate amounts of 99.8% purity raw materials of each element were weighed out for six buttons using a scale and grouped together in small plastic bags.

After sonicating the raw materials in methanol for fifteen minutes, the raw materials were placed in each of six wells in a water-cooled copper hearth in an arc melting machine, along with a titianium getter button. The chamber was sealed and pumped down to around 6mTorr before being backfilled with argon to 10.8 Torr. The titanium button was melted first for 1 minute at 250-300W to capture any remaining oxygen in the system. The arc was then directed at each of the six buttons for 30 seconds at 400W. Once cool, the buttons were flipped in the wells, and melted again to distribute the elements as evenly as possible. This was done one time. The buttons were removed and any oxides on the surface were ground off using a Dremel tool.

Making substrate. The six buttons were placed in a square mold copper hearth in the arc melter. The same pump down and titanium oxygen-capture process from above was followed again. The buttons were melted with a 650W arc into the square mold for at least 1 minute. Moving the arc stinger in a circular pattern around the surface of the molten metal helped to mix the contents more evenly.

The cooled substrate was milled to create a flat, $\frac{3}{4}$in surface for deposition. This surface was ground on an Allied polishing machine using silicon carbide sandpaper wheels to a 320 grit finish to create a surface for the deposited material to adhere.

Depositing Zr. The substrate was sonicated in methanol for 15 minutes before being placed in the laser chamber. The chamber was backfilled with argon gas. The DMC code used with the machine is included in Appendix B. A powder feedrate calibration was performed, the results of which are shown in Fig. 1.

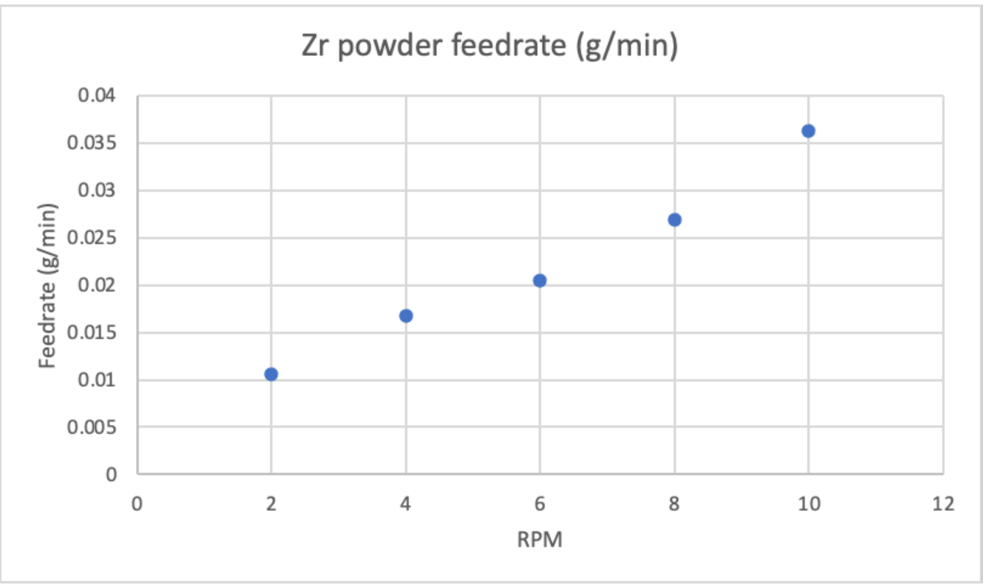

Figure 1 Feedrate calibration data.

The feedrate was set at 8RPM. The laser power was 250W and the travel speed of the laser varied between rows. Table 1 lists the travel speed at each row.

Table 1 Travel speeds of the laser at each row.

Row	1	2	3	4
Travel Speed (mm/s)	9.59	8.33	7.08	5.83

Each row consisted of 10 passes of the laser, each 0.5mm wide and overlapping its neighbors by approximately 50%. After the deposition, the rows were remelted at 180W and 2.5mm/s. The deposit surface was ground from 320 grit to 1200 grit by hand to avoid grinding through the deposited layers entirely. After 1200, the specimen was polished on a VibroMet polishing machine for 6 hours at a vibration amplitude of 60. A 0.02μm alumina particle polishing solution was used. Figure 2 shows the surfaces of the finished deposit before and after polishing.

(a) Raw deposit surface. **(b) Polished deposit surface.**

Figure 2 Deposit surfaces.

Hardness indentations. A Leitz diamond-tip Vickers microindenter was used in conjunction with a 108g mass to indent the polished surface of the specimen. Several indents were conducted across each row. The load on each indent was held constant for one minute. Images were taken of each indent using an optical microscope and can be seen in Appendix A. ImageJ was used to measure the diagonal width of each indent in μm. The Vickers hardness equation in Eq. 1 shows the formula used to derive the hardness values, in $\frac{kg}{mm^2}$, at each location:

$$HV = \frac{1.8544F}{gd^2} [8] \tag{1}$$

where g is the gravitational constant, d is the diameter of the indent, and F is the applied load in kg-f, found by multiplying the mass (108g, in this case) by g.

Microstructure analysis. The specimen was polished again for 3 hours in the VibroMet to remove any major lingering flaws in the surface, then sonicated in methanol 4 times and once in water for 5 minutes each to ensure no colloidal silica particles remained. Microstructural analysis was performed using a scanning electron microscope (SEM). Images were taken of two indents on each row at 5000x magnification to confirm that the obtained hardness values were representative of all phases present in the material. 15000x magnification was used to analyze one area near each indent. In addition to backscatter and secondary electron imaging, energy-dispersive X-ray spectroscopy (EDS) was performed at each focal point. Spectrums were obtained in estimation of the atomic percent composition of each location. The sampled locations were assumed to be representative of the entire row.

RESULTS & DISCUSSION

Microstructure Characterization. SEM images were taken using CBS and SED. Figure 3 shows one indent under secondary electron image.

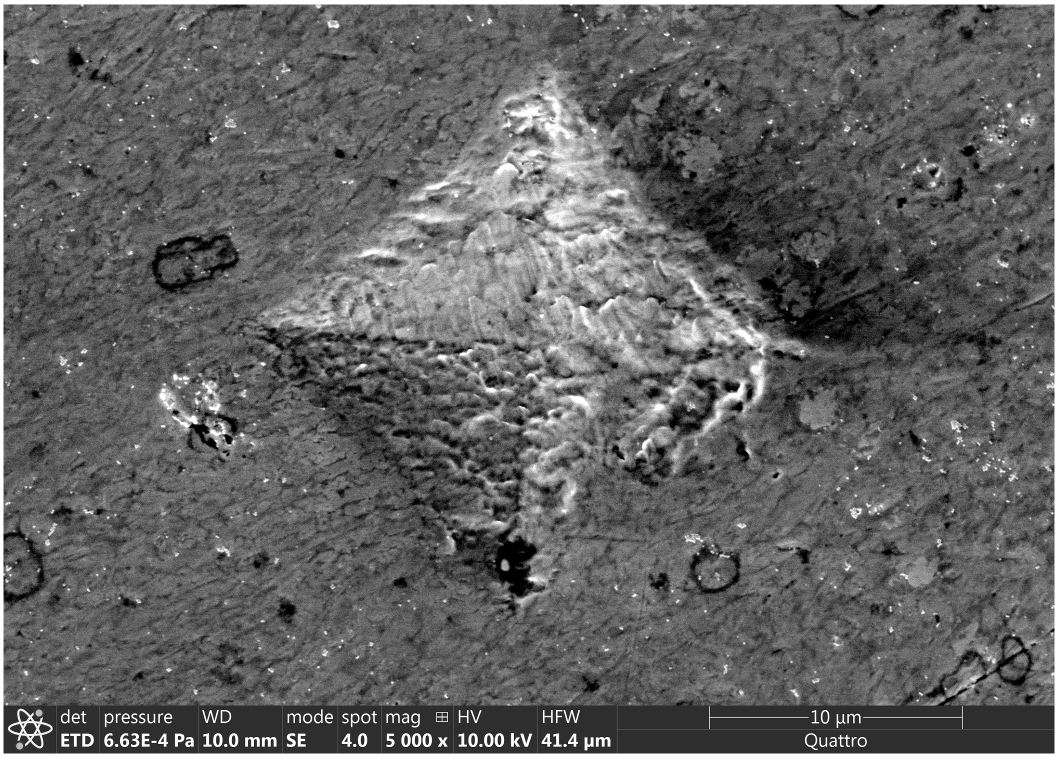

Figure 3 SEM secondary electron image showing a Vickers indent and microstructure on Row 4. Scale bar reads 10μm.

Images were also captured of the microstructures. Figures 3a-3j show the backscatter electron images captured, with EDS characterizations of the present elements. Zr is pink, Nb is red, and V is green (except for Fig. 3b, where Nb is pink, Zr is green, and V is red). Points 2 and 2a on Row 1 (3b and 3c) were taken near the same indent.

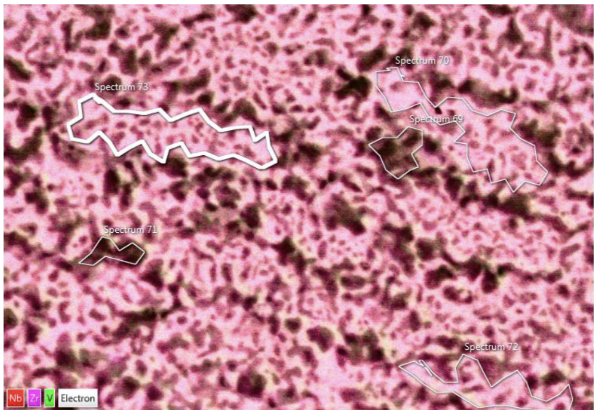

(a) Row 1 Point 1

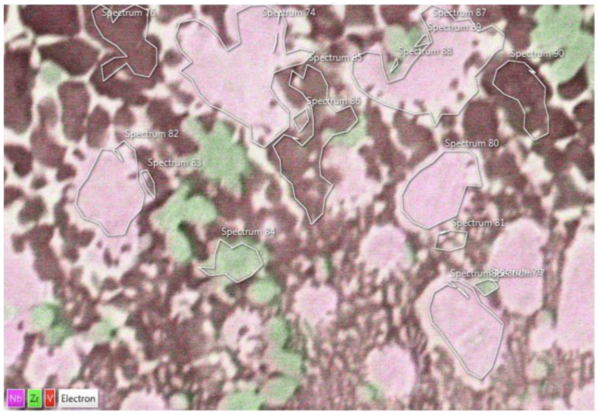

(b) Row 1 Point 2 (different colors)

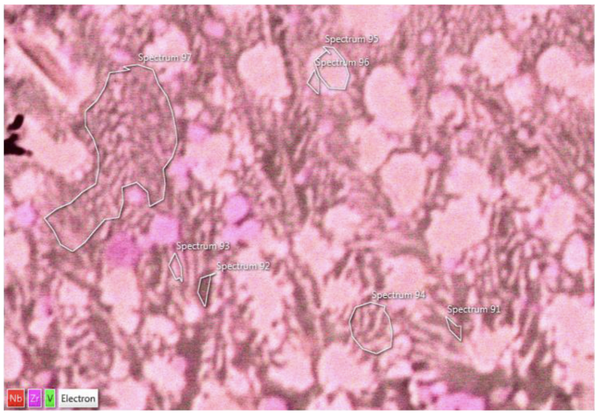

(c) Row 1 Point 2a

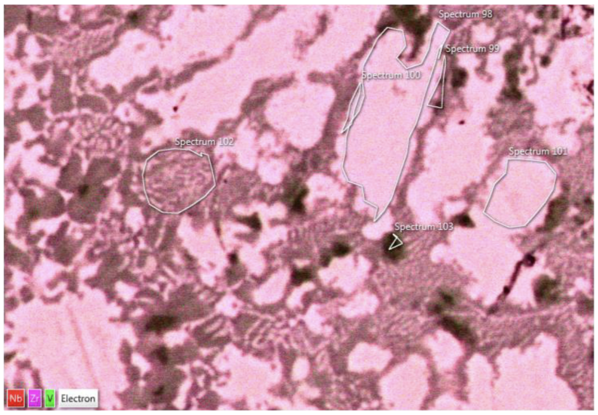

(d) Row 1 Point 3

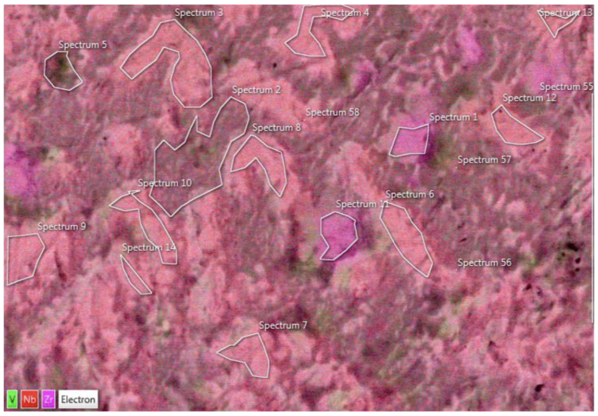

(e) Row 2 Point 1

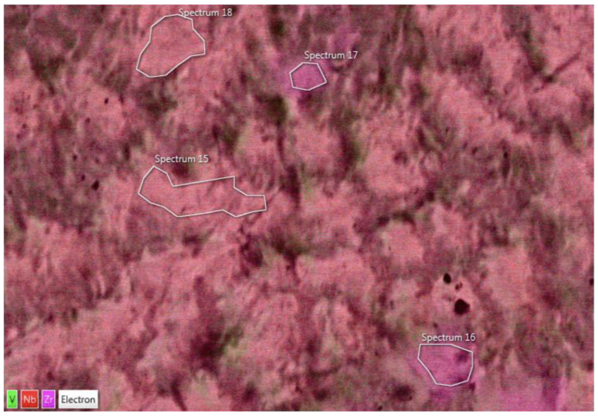

(f) Row 2 Point 2

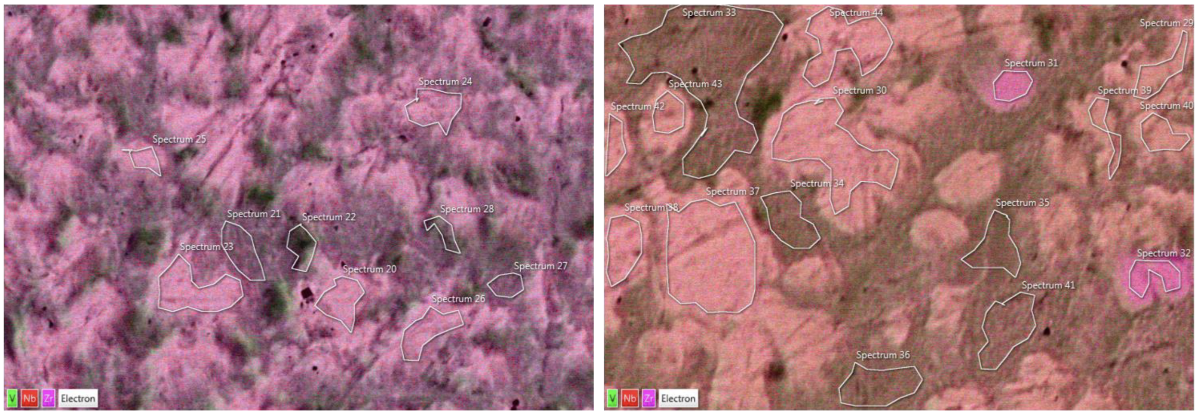

(g) Row 3 Point 1 **(h) Row 3 Point 2**

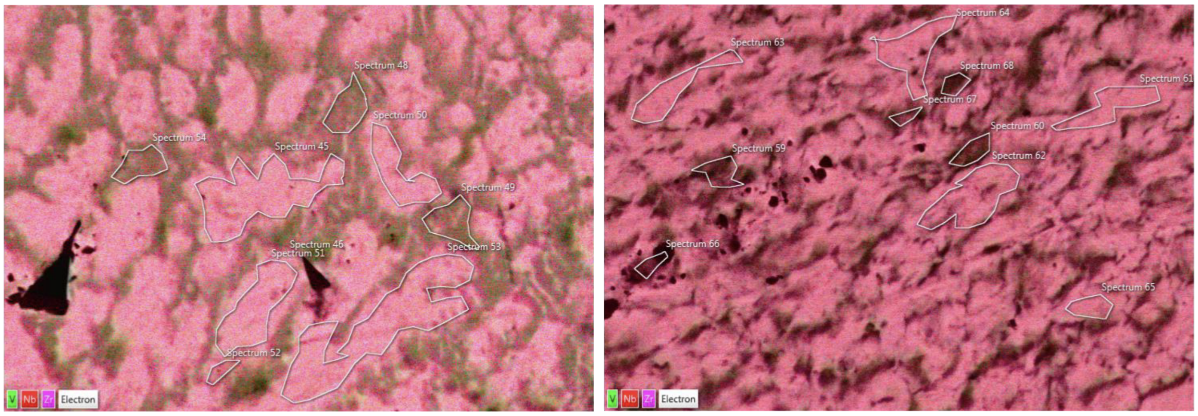

(i) Row 4 Point 1 **(j) Row 4 Point 2**

Figure 3 SEM backscatter images and EDS color spectrums captured of the microstructure at 2-3 points on each row. Images are 14 μm across.

There is a variety of different structures present across these images. The dendritic regions are identified by their more uniform, mostly pink appearance. In Row 1, there are layered structures in the interdendritic regions, with lots of Zr-rich regions. The density of the dendrites is smaller, except for Row 1 Point 1 in 3a. In that image, the structure seems more porous, with the dendrites having darker interdendritic regions incorporated within. The dendrites are often short or broken up, lacking the characteristic backbone-and-fingers structure. Some of the differences in structure within each row can be attributed to the location of each indent; Though the indents were placed as close to the middle of the laser pass track as possible, some of the indents may have been further from the middle and experienced different heat inputs and cooling rates. EDS spectroscopy analysis quantifies the visible phases. 109 spectrums were taken in total; 22 in Zr-rich regions, 29 in interdendritic regions, and 58 in the dendritic regions. Figure 4 shows bar charts of the at% composition of each phase and overall, including 10% error bars.

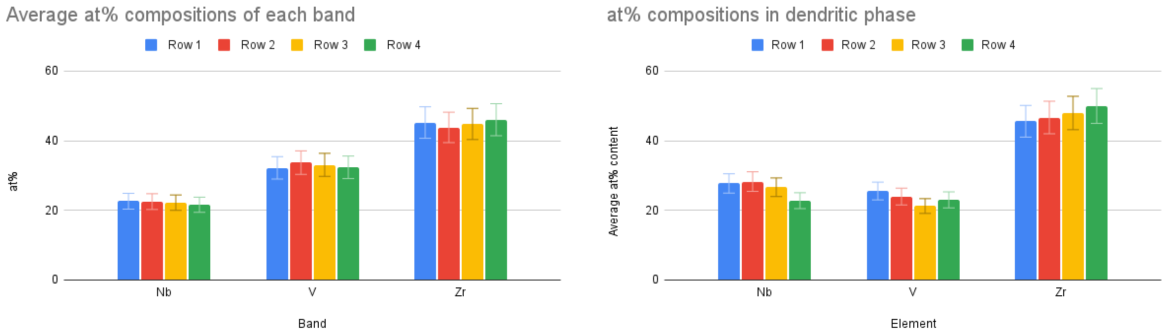

(a) Overall **(b) Dendritic**

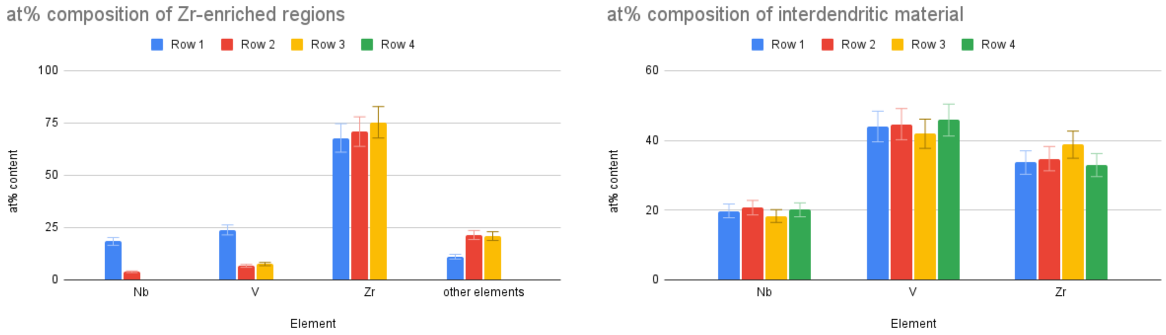

(c) Zr-enriched **(d) Interdendritic**

Figure 4 at% composition comparisons from EDS analysis of different visible phases on SEM across each row.

The error bars represent 10% error. Due to the inconsistent or inefficient nature of the deposition process, and accounting for possible analysis errors such as false identification, 10% was deemed an appropriate error margin.

In Figure 4c, there were no visible apparent Zr-enriched regions in Row 4, but there were significant contributions from elements such as oxygen and gold. The contribution from oxygen was 17.8% on average, and Row 1 Point 1 had 5.4% contribution from Au. The contributions from oxygen and gold are most likely inaccurate readings from the EDS analysis; it is probable that the spectrums falsely identified these materials because of the complex nature of the mixture of elements [9].

Overall, per Fig. 4a, as the changes between rows are all within the 10% error, the composition of the alloy stays roughly the same. As more Zr is added, the distributions of each element shift around, but the composition is not changing. Because of how much of the deposit surface was polished off in the sample preparation stage, it is actually possible that the surfaces analyzed here are more representative of the substrate's reaction to different laser travel speeds than any variation in Zr content.

According to Li's paper, an EBSD analysis of the ternary NbVZr alloy showed that the dendritic phase was a BCC solid solution, and the interdendritic phases were made of two Laves phases, with different ratios of the three elements [6]. The interdendritic phase here cannot be classified as Laves phase because it does not follow one of the reported stable metallic compound C14 or C15 Laves phase atomic formula of $[Nb_xZr_x]V_2$. Since there is no significant variation across rows, the average composition of the interdendritic phases across rows was found to be $Nb_{19.72}V_{44.08}Zr_{35.02}$, with the remaining composition accounted for by bigger fluctuations across the rows.

In the dendrites, as Zr increases, Nb and V generally decrease. Though this change falls within the error bars, suggesting the content isn't changing significantly, it still appears to follow a trend. This implies that Zr replaces the Nb and V in the dendritic phase as it gets deposited. The interdendritic phase composition also remains roughly constant across rows. This is more thoroughly explored later with the area fraction calculations.

Figure 4c displays an interesting pattern. The concentration of Zr-enriched regions apparent in each row seems to increase as Zr content increases, but once row 4 is reached, the regions cease to appear. Barring a sample size issue, such behavior may suggest that increasing the Zr content of the alloy destabilizes the Zr-enriched regions and reduces the present phases to just the dendrites and the interdendritic phase.

Hardness Characterization. An example of a Vickers indentation is shown in Fig. 5. This example indent was located on the third row from the top of the sample, Row 3.

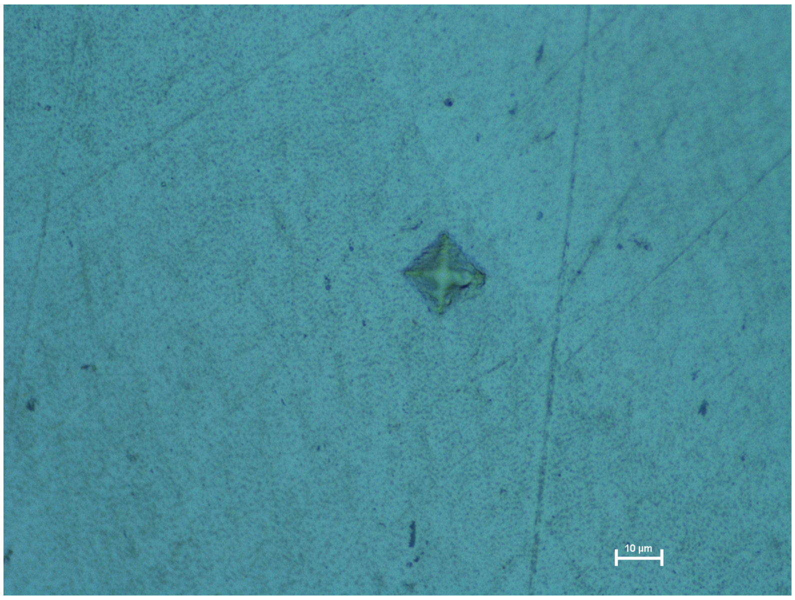

Figure 5 Vickers indent on Row 3. Scale bar reads 10μm.

The average measurements, on the Vickers hardness scale, of the indents collected across each row are presented in Table 2. Furthermore, assuming Eq. 2 is true:

$$HV = 3\sigma \tag{2}$$

where the hardness in $\frac{kg}{mm^2}$ is multiplied by gravitational constant to get it in units of $\frac{kgf}{mm^2}$, the mechanical strength of the material in each row can be estimated by dividing this value by 3.

Table 2 Average recorded Vickers hardnesses across each row.

Row	1	2	3	4
Laser Travel Speed (mm/s)	9.59	8.33	7.08	5.83
Hardness (kg/mm^2)	934.34	800.05	650.84	565.74
Strength (GPa)	3.054	2.615	2.127	1.849

The estimated strength is expected to lie in the range bounded by the yield strength and ultimate strength of the material [10]. These are extraordinarily high strengths for non-steel metal alloys, though some research has achieved Zr alloys with tensile strengths between 1 and 1.5 GPa [11]. Row 1 should theoretically have the lowest concentration of Zr as it had the fastest laser travel speed. The table shows a clear trend of decreasing hardness as the concentration of Zr increases. The SEM microstructure and area fraction analyses were important for more accurately analyzing this trend and identifying the present phases.

In the optical microscope, two phases were distinguishable. The darker phase, which looked like small speckles within the lighter phase, appeared to change in density as the Zr content increased from Row 1 to Row 4. Figure 6 shows optical microscope images of the surfaces of each row, with example images assumed to represent the appearance of the whole row.

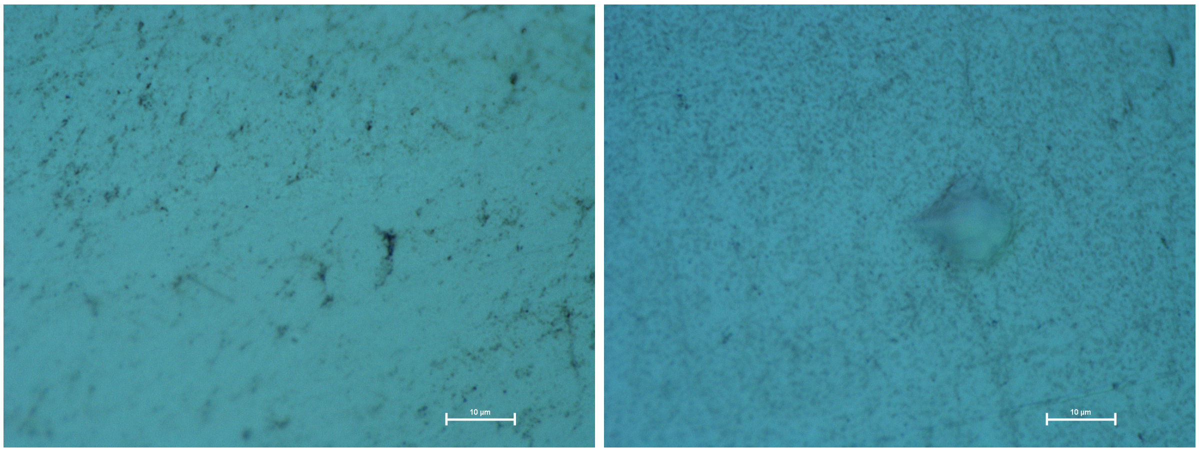

(a) Row 1 surface on optical microscope. **(b) Row 2 surface on optical microscope.**

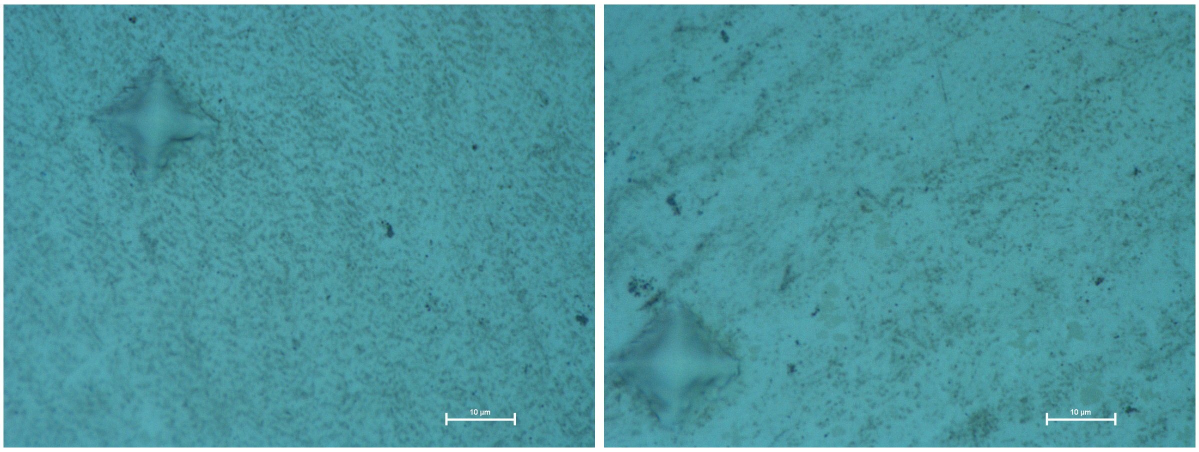

(c) Row 3 surface on optical microscope. **(d) Row 4 surface on optical microscope.**

Figure 6 Representative example optical microscope images of surfaces of each row. Scale bars read 10μm.

The Optical microscope images of all four rows can be found in the Appendix. In the optical microscope, two phases were distinguishable. The darker phase, which looked like small speckles within the lighter phase, appeared to change in density as the Zr content increased from Row 1 to Row

4. These images confirmed that the Vickers indents were sampling the material as a whole, rather than one phase or another, as it is clear that both phases got incorporated into the indent.

Area Fractions. In addition to the SEM/EDS composition analysis, the average area fraction occupied by the dendrites in each row was calculated. Figure 7 shows how the images were analyzed to achieve this, and Table 3 shows these values.

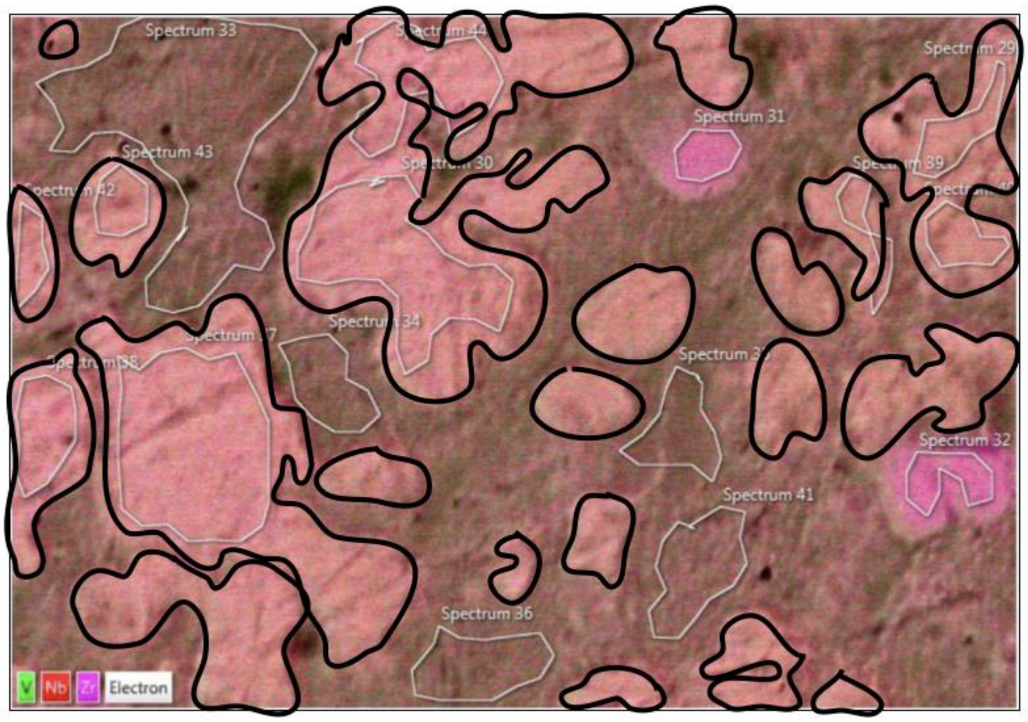

Figure 7 Example image of area fraction calculations for dendritic regions (Row 3 point 2), featuring spectroscopy analysis areas outlined in white.

Also visible in this image are the white outlines where different EDS spectrums were taken. The hot pink areas are examples of how Zr-rich regions appeared in the spectrum analyses. ImageJ was used to find the area enclosed in each black shape (the dendrites), and then the sum of the areas was taken and divided by the total area of the photo. These values were averaged across each row.

Table 3 Dendritic area fractions by row.

Row 1	Row 2	Row 3	Row 4
0.212	0.304	0.356	0.545

There is a clear increase in area fraction of dendrites present as Zr increases. Since the only other primarily present phase is the interdendritic phase, this also corresponds to a decrease in the presence of the interdendritic phase. The dendritic area fractions are plotted against the hardness values from Table 2 in Fig. 8.

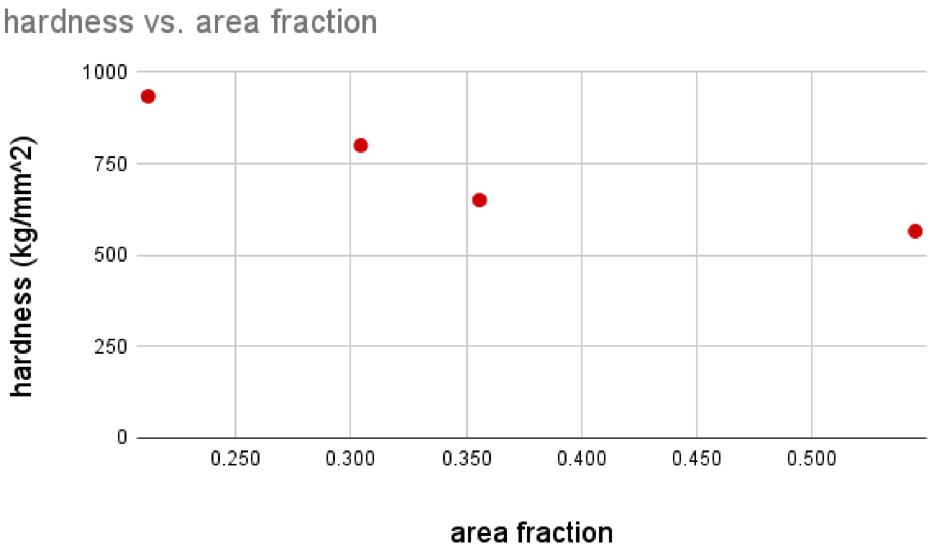

Figure 8 **Dendritic area fraction of the rows against hardness in kg/mm^2.**

As shown in the figure, there is a direct negative relationship between dendritic area fraction and hardness values of each row. This says that increasing the dendritic phase makes the alloy less hard, suggesting that the dendritic phase is the softer one.

Li's work found that adding Nb stabilized both the interdendritic Laves phases by replacing Zr in the Laves structure [6]. Research by Sam Ehrman, performed and written in conjunction with this work, explores the addition of Nb to the same NbVZr ternary alloy, and will be referenced in comparison [7]. Because of this relationship between Nb and Zr, it follows that by increasing Zr instead, the interdendritic phase would be destabilized. This explains the decrease in the area fraction occupied by the interdendritic phase by way of increasing the dendritic area fraction. Further conclusions in the same body of work indicate that a greater abundance of the Laves phases resulted in an increase in hardness; it was found that by acting as an obstacle to dislocation motion in the dendritic phase the Laves phase strengthened the BCC phase [6]. Though the interdendritic phases here cannot be classified as Laves phases, it still appears that they serve the same purpose as the Laves phases did in Li's work, impeding dislocation motion in the dendritic phase and strengthening the material overall.

As mentioned above, the observed structures could be more representative of the effects of laser travel speed, though the two should theoretically be interrelated. As the laser travel speed decreases (Row 1 being fastest), the dendritic area fraction increases. This may likely be a result of different cooling speeds; slower travel speeds force the molten metal to cool slower, allowing coarser dendrites to grow and resulting in less abundant interdendritic phases. Since the dendrites are the softer phase, coarser dendrites would make the hardness of the material decrease.

Regardless of the mechanism behind the increase in the area fraction of dendritic phase present, it follows that Row 4 should have a lower hardness than Row 1, and this is supported by Table 2 and Fig. 8.

From Fig. 4d it is clear that the composition of the interdendritic phase doesn't change, but from Table 3 it becomes clear that the quantity of the phase does decrease. It suggests that Zr, in addition to possibly being a destabilizer for Zr-rich regions, also destabilizes the interdendritic phase. Instability makes the interdendritic phase difficult to form, so the solid solution phase in the disordered dendrites become the preferential phase with more Zr content. At the lower concentrations of Zr in Row 1 (Fig. 3a-3d), the dendrites are actually surrounded by small areas of nearly 100% Zr. The Zr in these regions has pooled around the edges of the dendrites. This could be the result of a number of things. It may be possible that the pooled Zr is another version of the Zr-enriched phase that appears; this would make sense if, in fact, increasing the Zr content of the alloy destabilizes that phase. More thorough exploration would be needed to determine whether the driver of these trends is the cooling rate/laser travel speed or the variance in Zr content. Further research could explore whether adding more Zr to the alloy could result in a singular BCC phase material.

While the observed at% composition offers a view of the general behaviors of the alloy, it cannot be fully relied on for a number of reasons. There were several sampled spectrums that picked up elements such as oxygen, phosphorous, and gold, in varying quantities; these spectrums are unreliable because the actual overall composition of the ternary elements is inconclusive. Additionally, some locations were sampled more than others due to operational constraints.

Comparison to Nb-deposit sample. As mentioned, another paper written by Sam Ehrman explores the behavior of the ternary NbVZr alloy with the addition of Nb [7]. When this Zr-deposit sample is compared with the Nb-deposit sample, a few prominent similarities arise. First, in both iterations, the Nb was concentrated in the dendrites, and appeared only sparsely in the interdendritic regions. Li's paper determines the composition of one Laves phase to follow the form $NbZr_3V_8$ [6]. While the obtained composition values don't follow this form exactly, there is somewhat similar behavior with the magnitudes of each element's presence. V is significantly higher than both Zr and Nb in the interdendritic region, and Nb falls at around half of the Zr content as well. In the Nb deposition, the Nb and Zr were roughly equal in content in the interdendritic regions. This makes sense because there would be more Nb present overall in that sample. Li says that the composition for the associated Laves phase is similar to $Nb_5Zr_3V_{16}$ [6]. Because of Nb's heavy preference for the dendritic phase, it stands to reason that Nb is the driver of the dendritic solid-solution phase, meaning Nb content controls the formation of the BCC phase. For the Zr sample, more Zr was not incorporated at lower laser travel speeds; the only change was the travel speed itself, which affected the cooling rate, which did not change the composition of the dendrites. For the Nb sample, increasing Nb altered the dendritic composition.

A difference is the presence of Zr-enriched regions. The Nb sample consistently saw small regions that were higher in Zr. In the Zr sample, such regions were between 60-70% Zr, while in the Nb sample, the composition was closer to 40-50% Zr. Because the Nb sample did not add Zr, the Zr-rich regions were not forced out of stability, and the distinct structures were able to remain. The elements in the Nb sample tend to favor separation. This leads to the idea that Zr could be the driver of mixing for the alloy. This is also supported by the large presence of Zr in every phase in the Zr sample, as well as a reasonably large presence in the Nb phase. The high-Zr phases in the Nb sample are similar in composition to the dendritic phase in the Zr sample: 29.5% Nb, 24.4% V, and 46.1% Zr, compared to 28.1% Nb, 23.4% V, and 47.5% Zr respectively. This similarity suggests that there is an ordered composition to the dendritic phase in the Zr sample (or the high-Zr phase in the Nb sample).

It is possible, based on these comparisons, that the presence of Zr drives up the entropy of the alloy. Figures 9a and 9b show ternary system contour plots representing different qualities of the alloy.

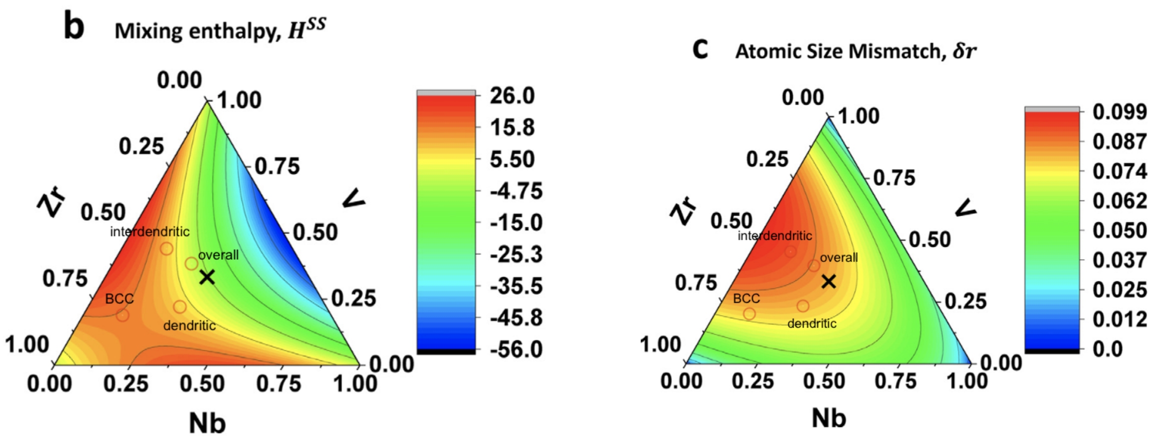

(a) Ternary plot of mixing enthalpy changing with composition.

(b) Ternary plot of how atomic mismatches change with composition.

Figure 9 Ternary plots of mixing enthalpy H^{SS} and atomic size mismatch δr.

For the formation of a single-phase BCC solid solution, the expected value of δH is expected to fall in the range of -15 to 5 kJ/mol [6]. The ternary diagram in Fig. 9a shows that the interdendritic phase on the Zr sample has higher mixing enthalpy than the equiatomic substrate does. The position of the interdendritic phase on this diagram says that the enthalpy should be around 8-11 kJ/mol. This is greater than the equiatomic overall value, which is around 0 kJ/mol. This difference is negative; according to Li, this means that the phase is stable [6]. However, since it falls outside of the single-phase range of δH, there should not be any solid solution in this phase, which follows with the results in Fig. 3. Similar things can be said for the dendritic structure and the Zr-enriched phase (mislabeled as BCC) which have mixing enthalpies of 2-6 kJ/mol and 15-20 kJ/mol, respectively. The interdendritic and dendritic phases in particular have almost identical mixing enthalpies. This diagram suggests that all of the phases present are stable while they exist, but that no single-phase BCC solid solution was formed.

In the Nb-deposit, the mixing enthalpies of each corresponding phase was lower than that of the Zr-deposit, falling closer towards the green and yellow areas within the range of the BCC expected value of δH. For the Nb-rich dendrites in this sample, the mixing enthalpy was around -12 kJ/mol, which falls within the range where a single-phase BCC solid solution is expected to appear. It can be said, therefore, that this dendritic phase was a BCC solid solution, based on the mixing enthalpies.

With atomic size mismatch, the necessary condition for the formation of a solid solution phase is $\delta r \leq 6.6\%$ [6]. Below Above this value, there is higher chance for the single solid solution to emerge [12]. The interdendritic phase has a very high δr of about 9%, while the Zr-rich and dendritic phases are comparable to the overall composition value of 7.5-8.5%. Because the values lie above the threshhold for solid solution BCC phase to form, it is not expected that some would be visible across the rows, and it predicts the presence of intermetallic compounds [6], which follow with the interdendritic phases present throughout.

In the Nb sample, the dendritic phase falls in the range of $6.5\% \leq \delta r \leq 7\%$ atomic mismatch. This could potentially foster the formation of the BCC solid solution, if it is on the lowest end of the range. However, the other phases fall into the orange and red areas on the ternary plot, with $\delta r \geq 8\%$ [7], so there is not expected to be any solid solution in any of those phases.

CONCLUSION

This report aimed to characterize the behavior of a ternary NbVZr alloy with varying amounts of Zr added using a laser deposition process. A decrease in hardness was observed as travel speed decreased, from 934 HV to 565 HV. This was accompanied by a microstructural analysis through SEM imaging and EDS spectroscopy, which found dominant dendritic and interdendritic phases alongside a weaker Zr-rich phase. The average overall composition of the rows was found to be relatively consistent, suggesting that the change in laser travel speed did not affect the incorporation of more Zr. The Zr-rich phase appeared to become destabilized by the quantity of Zr present, decreasing in frequency of appearance as Zr increased before disappearing completely from Row 4.

The interdendritic phase also appeared to be destabilized by the increase in Zr. The dendrites were found to increase in area fraction with Zr content. This meant that there was less interdendritic phase present. This could also suggest that more Zr would increase the amount of BCC solid solution phase present, perhaps even producing a material comprised of a single BCC phase. Future research can pursue this theory, or explore what effects adding different elements might have.

Similar trends were observed in the Nb sample. However, one notable difference was the consistent presence of three phases, and the distinct separation of the three elements into these phases. Both samples saw interdendritic phases rich in V, and dendrites that were rich in Nb. The Nb sample's dendrites contained much more Nb. A third phase was the Zr-rich regions. Because the Zr content was not increasing in the Nb sample, the Zr-rich phase was not destabilized and remained present across all four rows.

Analysis on ternary diagrams for mixing enthalpy and atomic size mismatch also helped characterize the responses of each sample. It was found that the Zr-deposit sample likely had stable phases, but was not expected to produce any single-phase BCC solid solution in any of the regions. In the Nb-deposit sample, the dendritic regions were within the H^{SS} threshold for the formation of the single-phase BCC solid solution, but were right at or just above the maximum threshold for δr, so it was unclear whether this phase could be classified as BCC solid solution. The other phases present in the Nb-deposit sample did not meet the requirements in either diagram.

The dendritic phase of the Zr sample was estimated to be $Nb_{28.17}V_{23.17}Zr_{47.53}$ by atomic percent. The remaining two percent may be attributed to trace elements like oxygen and carbon, potentially from oxidation on the surface of the deposits.

Future experiments following this work may choose to explore the effects of changing the powder feedrate of the Zr deposit, rather than the laser travel speed, to more directly measure any potential change in composition. It would also be interesting to research getting a composition of the ternary alloy to fall within the thresholds of all the criteria for the formation of the BCC single-phase solid solution.

References

[1] Murty, B., Yeh, J.-W., Ranganathann, S., and Bhattacharjee, P., 2019, *High-Entropy Alloys*, 2nd ed., Elsevier.

[2] Yen, H., Yeh, A.-C., and Yeh, J.-W., 2024, "High-entropy alloys: An overview on the fundamentals, development, and future perspective," *Encyclopedia of Condensed Matter Physics (Second Edition)*, Second edition ed., T. Chakraborty, ed., Academic Press, pp. 647–658, doi: https://doi.org/10.1016/B978-0-323-90800-9.00117-7, https://www.sciencedirect.com/science/article/pii/B9780323908009001177

[3] Zhang, Z., Li, M., Cavin, J., Flores, K., and Mishra, R., 2022, "A Fast and Robust Method for Predicting the Phase Stability of Refractory Complex Concentrated Alloys using Pairwise Mixing Enthalpy," Acta Materialia, **241**, p. 118389.

[4] Tsai, M.-H. and Yeh, J.-W., 2014, "High-Entropy Alloys: A Critical Review," Materials Research Letters, **2**(3), pp. 107–123.

[5] Lusi and Matteo, 2018, "Engineering Crystal Properties through Solid Solutions," Crystal Growth & Design, **18**(6), pp. 3704–3712.

[6] Li, M., Zhang, Z., Thind, A. S., Ren, G., Mishra, R., and Flores, K. M., 2021, "Microstructure and properties of NbVZr refractory complex concentrated alloys," Acta Materialia, **213**, p. 116919.

[7] Ehrman, S. and Flores, K. M., 2024, "Ternary NbVZr alloy," Tech. rep., Washington University in St. Louis.

[8] Zhang, H. W., Subhash, G., Jing, X. N., Kecskes, L. J., and Dowding, R. J., 2006, "Evaluation of hardness–yield strength relationships for bulk metallic glasses," Philosophical Magazine Letters, **86**(5), pp. 333–345.

[9] Reed, S. J., 1995, "Introduction to Energy Dispersive X-ray Spectrometry (EDS)," Tech. rep., Central Facility for Advanced Microscopy and Microanalysis at University of California, Riverside.

[10] Zhang, P., Li, S., and Zhang, Z., 2011, "General relationship between strength and hardness," Materials Science and Engineering: A, **529**, pp. 62–73.

[11] Zhang, N., Xia, C., Qin, J., Li, Q., Zhang, X., and Riu, R., 2022, "Research progress of novel zirconium alloys with high strength and toughness," Journal of Metals, Materials and Minerals, **32**, pp. 23–36.

[12] Zhao, K., Benton, A., Xu, F., Shi, X., , and He, J., 2021, "Atomic size mismatch: What if it is too large?" Matter, **4**, pp. 2582–2685.

List of Figures

List of Tables

A Raw Data

Tables A.1, A.2, A.3, and A.4 show the compositions of each phase across the rows. This is the same data from Figure 4.

Table A.1 **at% compositions of Nb, V, and Zr overall.**

	Row 1	Row 2	Row 3	Row 4	Average
Nb	22.625	22.5	22.2	21.6	22.23
V	32.175	33.7	33.05	32.4	32.83
Zr	45.2	43.8	44.8	46.0	44.95

Table A.2 **at% compositions of Nb, V, and Zr in dendritic phase.**

	Row 1	Row 2	Row 3	Row 4	Average
Nb	35.01	28.25	26.62	22.78	28.17
V	25.54	23.96	21.22	23.01	23.43
Zr	45.57	46.65	47.93	49.95	47.52

Table A.3 **at% compositions of Nb, V, and Zr in Zr-enriched phase.**

	Row 1	Row 2	Row 3	Row 4
Nb	18.38	3.9	0	0
V	23.88	6.73	7.6	0
Zr	67.81	70.85	75.3	0
Other elements	11.1	21.475	20.9	0

Table A.4 at% compositions of Nb, V, and Zr in interdendritic phase.

	Row 1	**Row 2**	**Row 3**	**Row 4**
Nb	19.77	20.7	18.3	20.09
V	43.97	44.65	41.9	45.81
Zr	33.64	34.75	38.76	32.91

Table A.5 compares the averages of the compositions.

Table A.5 Average compositions across rows for each phase.

	overall	dendritic	Zr-enriched	interdendritic
Nb	32.83	28.17	11.14	19.72
V	33.08	23.43	12.74	44.08
Zr	44.95	47.53	53.49	35.02

Link to box folder or go to https://wustl.box.com/s/7fkpnx6pnwwwsfcdhnn90r4u7vilm9tz This folder contains all SEM images, optical microscope images, and calculations performed.

B DMC Code For Deposition

```
REM SLICE1 PWR  35.0 PF1=1
REM SLICE2 PWR  35.0 PF2=2
REM SLICE PWR   END
REM ***************************************************************************
REM C:\Documents and ...
    Settings\Administrator\Desktop\Square_Array_12x12_200ms_Remelt.DMC
REM ***************************************************************************
REM ********** Convert Slice to DMC Process Parameters **********
REM Layer Thickness = 0.008
REM Resolution = 5000
REM Contour Feedrate = 40
REM X Axis Resolution = 200000
REM Y Axis Resolution = 200000
REM Z Axis Resolution = 200000
REM Laser On Feedrate = 40
REM Laser On Accel = 60000
REM Laser On Decel = 60000
REM Laser On Shutter Delay = 20
REM Laser Off Feedrate = 60
REM Laser Off Accel = 60000
REM Laser Off Decel = 60000
REM Laser Off Shutter Delay = 20
REM *************************************************************
REM Hatches For Layer 2 (Ti)
DP 0,0,0
AC 3000000, 3000000, 3000000
DC 3000000, 3000000, 3000000
SP 50000, 50000, 50000

REM ====================NEW ROW=====================================

REM Hatch 1x1

PA 0,0
BG XY
```

```
AM XY
VM XY
VA 3000000
VD 3000000
VS 191693
VP 112974,0
VE
SB1
WT 20
BGS
AMS
CB 1
WT 30

PA 112974,1750
BG XY
AM XY
VM XY
VA 3000000
VD 3000000
VS 191693
VP -112974,0
VE
SB1
WT 20
BGS
AMS
CB 1
WT 30

PA 0,3500
BG XY
AM XY
VM XY
VA 3000000
VD 3000000
VS 191693
VP 112974,0
```

```
VE
SB1
WT 20
BGS
AMS
CB 1
WT 30

PA 112974,5249
BG XY
AM XY
VM XY
VA 3000000
VD 3000000
VS 191693
VP -112974,0
VE
SB1
WT 20
BGS
AMS
CB 1
WT 30

PA 0,6999
BG XY
AM XY
VM XY
VA 3000000
VD 3000000
VS 191693
VP 112974,0
VE
SB1
WT 20
BGS
AMS
CB 1
```

```
WT 30

PA 112974,8749
BG XY
AM XY
VM XY
VA 3000000
VD 3000000
VS 191693
VP -112974,0
VE
SB1
WT 20
BGS
AMS
CB 1
WT 30

PA 0,10499
BG XY
AM XY
VM XY
VA 3000000
VD 3000000
VS 191693
VP 112974,0
VE
SB1
WT 20
BGS
AMS
CB 1
WT 30

PA 112974,12248
BG XY
AM XY
VM XY
```

```
VA 3000000
VD 3000000
VS 191693
VP -112974,0
VE
SB1
WT 20
BGS
AMS
CB 1
WT 30

PA 0,13998
BG XY
AM XY
VM XY
VA 3000000
VD 3000000
VS 191693
VP 112974,0
VE
SB1
WT 20
BGS
AMS
CB 1
WT 30

PA 112974,15748
BG XY
AM XY
VM XY
VA 3000000
VD 3000000
VS 191693
VP -112974,0
VE
SB1
```

```
WT 20
BGS
AMS
CB 1
WT 30

WT 20000
REM Hatch 2x1

PA 0,23000
BG XY
AM XY
VM XY
VA 3000000
VD 3000000
VS 166693
VP 112974,0
VE
SB1
WT 20
BGS
AMS
CB 1
WT 30

PA 112974,24750
BG XY
AM XY
VM XY
VA 3000000
VD 3000000
VS 166693
VP -112974,0
VE
SB1
WT 20
BGS
AMS
```

```
CB 1
WT 30

PA 0,26500
BG XY
AM XY
VM XY
VA 3000000
VD 3000000
VS 166693
VP 112974,0
VE
SB1
WT 20
BGS
AMS
CB 1
WT 30

PA 112974,28250
BG XY
AM XY
VM XY
VA 3000000
VD 3000000
VS 166693
VP -112974,0
VE
SB1
WT 20
BGS
AMS
CB 1
WT 30

PA 0,30000
BG XY
AM XY
```

```
VM XY
VA 3000000
VD 3000000
VS 166693
VP 112974,0
VE
SB1
WT 20
BGS
AMS
CB 1
WT 30

PA 112974,31750
BG XY
AM XY
VM XY
VA 3000000
VD 3000000
VS 166693
VP -112974,0
VE
SB1
WT 20
BGS
AMS
CB 1
WT 30

PA 0,33500
BG XY
AM XY
VM XY
VA 3000000
VD 3000000
VS 166693
VP 112974,0
VE
```

```
SB1
WT 20
BGS
AMS
CB 1
WT 30

PA 112974,35250
BG XY
AM XY
VM XY
VA 3000000
VD 3000000
VS 166693
VP -112974,0
VE
SB1
WT 20
BGS
AMS
CB 1
WT 30

PA 0,37000
BG XY
AM XY
VM XY
VA 3000000
VD 3000000
VS 166693
VP 112974,0
VE
SB1
WT 20
BGS
AMS
CB 1
WT 30
```

```

PA 112974,38750
BG XY
AM XY
VM XY
VA 3000000
VD 3000000
VS 166693
VP -112974,0
VE
SB1
WT 20
BGS
AMS
CB 1
WT 30

WT 20000
REM Hatch 3x1

PA 0,46000
BG XY
AM XY
VM XY
VA 3000000
VD 3000000
VS 141693
VP 112974,0
VE
SB1
WT 20
BGS
AMS
CB 1
WT 30

PA 112974,47750
BG XY
```

```
AM XY
VM XY
VA 3000000
VD 3000000
VS 141693
VP -112974,0
VE
SB1
WT 20
BGS
AMS
CB 1
WT 30

PA 0,49500
BG XY
AM XY
VM XY
VA 3000000
VD 3000000
VS 141693
VP 112974,0
VE
SB1
WT 20
BGS
AMS
CB 1
WT 30

PA 112974,51250
BG XY
AM XY
VM XY
VA 3000000
VD 3000000
VS 141693
VP -112974,0
```

```
VE
SB1
WT 20
BGS
AMS
CB 1
WT 30

PA 0,53000
BG XY
AM XY
VM XY
VA 3000000
VD 3000000
VS 141693
VP 112974,0
VE
SB1
WT 20
BGS
AMS
CB 1
WT 30

PA 112974,54750
BG XY
AM XY
VM XY
VA 3000000
VD 3000000
VS 141693
VP -112974,0
VE
SB1
WT 20
BGS
AMS
CB 1
```

```
WT 30

PA 0,56500
BG XY
AM XY
VM XY
VA 3000000
VD 3000000
VS 141693
VP 112974,0
VE
SB1
WT 20
BGS
AMS
CB 1
WT 30

PA 112974,58250
BG XY
AM XY
VM XY
VA 3000000
VD 3000000
VS 141693
VP -112974,0
VE
SB1
WT 20
BGS
AMS
CB 1
WT 30

PA 0,60000
BG XY
AM XY
VM XY
```

```
VA 3000000
VD 3000000
VS 141693
VP 112974,0
VE
SB1
WT 20
BGS
AMS
CB 1
WT 30

PA 112974,61750
BG XY
AM XY
VM XY
VA 3000000
VD 3000000
VS 141693
VP -112974,0
VE
SB1
WT 20
BGS
AMS
CB 1
WT 30

WT 20000
REM Hatch 4x1

PA 0,69000
BG XY
AM XY
VM XY
VA 3000000
VD 3000000
VS 116693
```

```
VP 112974,0
VE
SB1
WT 20
BGS
AMS
CB 1
WT 30

PA 112974,70750
BG XY
AM XY
VM XY
VA 3000000
VD 3000000
VS 116693
VP -112974,0
VE
SB1
WT 20
BGS
AMS
CB 1
WT 30

PA 0,72500
BG XY
AM XY
VM XY
VA 3000000
VD 3000000
VS 116693
VP 112974,0
VE
SB1
WT 20
BGS
AMS
```

```
CB 1
WT 30

PA 112974,74250
BG XY
AM XY
VM XY
VA 3000000
VD 3000000
VS 116693
VP -112974,0
VE
SB1
WT 20
BGS
AMS
CB 1
WT 30

PA 0,76000
BG XY
AM XY
VM XY
VA 3000000
VD 3000000
VS 116693
VP 112974,0
VE
SB1
WT 20
BGS
AMS
CB 1
WT 30

PA 112974,77750
BG XY
AM XY
```

```
VM XY
VA 3000000
VD 3000000
VS 116693
VP -112974,0
VE
SB1
WT 20
BGS
AMS
CB 1
WT 30

PA 0,79500
BG XY
AM XY
VM XY
VA 3000000
VD 3000000
VS 116693
VP 112974,0
VE
SB1
WT 20
BGS
AMS
CB 1
WT 30

PA 112974,81250
BG XY
AM XY
VM XY
VA 3000000
VD 3000000
VS 116693
VP -112974,0
VE
```

```
SB1
WT 20
BGS
AMS
CB 1
WT 30

PA 0,83000
BG XY
AM XY
VM XY
VA 3000000
VD 3000000
VS 116693
VP 112974,0
VE
SB1
WT 20
BGS
AMS
CB 1
WT 30

PA 112974,84750
BG XY
AM XY
VM XY
VA 3000000
VD 3000000
VS 116693
VP -112974,0
VE
SB1
WT 20
BGS
AMS
CB 1
WT 30
```

```
WT 20000
```

List of Figures

List of Tables